



Role of non-magnetic dopants (Ca, Mg) in GdFeO₃ perovskite nanoparticles obtained by different synthetic methods: structural, morphological and magnetic properties

Antonia Ruffo¹, Maria Cristina Mozzati², Benedetta Albini², Pietro Galinetto², and Marcella Bini^{1,*}

¹Department of Chemistry, University of Pavia, viale Taramelli 16, 27100 Pavia, Italy

²Department of Physics, University of Pavia, via Bassi 6, 27100 Pavia, Italy

Received: 10 June 2020

Accepted: 27 August 2020

© The Author(s) 2020

ABSTRACT

GdFeO₃ perovskite attracted large interest in different fields thanks to peculiar magnetic and optical properties that are further tunable by means of doping processes and achievable on both Gd and Fe sites or by properly choosing the synthesis routes. In this paper, nanometric GdFeO₃ compounds, undoped and doped with diamagnetic Ca²⁺ and Mg²⁺ ions, were synthesized by microwave assisted, sol-gel, and polyol syntheses and characterized by X-ray diffraction, showing solid solutions formation. Raman spectroscopy allowed us to confirm, from peak enlargements, the Ca and Mg substitution on Gd and Fe sites, respectively. The magnetic data showed the presence of magnetic domains as consequence of doping with diamagnetic ions, which seem to play a crucial role in the magnetic activity of the compounds. A superparamagnetic behaviour is evidenced; nevertheless, its intrinsic character is not definitely demonstrated. Indeed, the possible presence of traces of magnetic impurities, which are easily obtainable in these samples, such as iron oxides, must be taken into account.

1 Introduction

GdFeO₃ is one of the most important members of the lanthanide metal oxide perovskites ABO₃ (A = La, Sm, Eu, Gd) class. An ideal perovskite has a cubic crystal structure, composed of a three-dimensional framework of corner-sharing BO₆ octahedra. It was

demonstrated that the formation of regular perovskites is mainly governed by the Goldschmidt “tolerance factor” ($t = r_A + r_O / \sqrt{2(r_B + r_O)}$), where r_A , r_B , and r_O are the ionic radii of A, B, and O atoms, respectively [1]. The t value of an ideal perovskite should be equal to 1.0, even if, based on the analysis of tolerance factor values, the perovskite structure is hexagonal, cubic, and orthorhombic for

Address correspondence to E-mail: bini@unipv.it

$1.00 < t < 1.13$, $0.9 < t < 1.0$, and $0.75 < t < 0.9$, respectively. It seems, however, that proper t values are a necessary, but not a sufficient condition for the formation of the perovskite structure. In addition, the octahedron BO_6 , i.e. the basic unit for perovskite structure, has a great importance and an "octahedral factor" can be defined as r_B/r_O . By considering both these factors, the perovskites formability can be reliably predicted. GdFeO_3 with a t value of 0.86 crystallizes in the orthorhombic space group $Pnma$ showing a distorted perovskite-type structure, as a result of the FeO_6 octahedra tilting, with Gd^{3+} in a eightfold coordination [1, 2]. GdFeO_3 is one among the few known multiferroic perovskites crystallizing in orthorhombic structure [3, 4]. Its overall magnetic behaviour is described as the result of two contributing magnetic 'sublattices': (i) an antiferromagnetic iron oxide lattice in which the spins are coupled via an $\text{Fe}^{3+}-\text{O}^{2-}-\text{Fe}^{3+}$ super-exchange mechanism and (ii) a paramagnetic contribution from essentially non-coupled Gd^{3+} ions. Fe spins ($S = 5/2$) order antiferromagnetically at the Néel temperature $T(\text{Fe}) \cong 660$ K and a weak ferromagnetic moment is observed due to the spin-canting associated to the Dzyaloshinskii–Moriya interactions in the iron-containing sublattice, as a result of the distorted perovskite structure [5–11]. The distinctive feature of GdFeO_3 is above room temperature: indeed, it is not only a weak ferromagnet, but also displays a ferroelectric ground state, in which the ferroelectric polarization is generated by the striction through the exchange interaction between the Gd and Fe spins [7, 12–14]. Due to the source of polarization, GdFeO_3 is considered an improper multiferroic system. From the optical point of view, GdFeO_3 is a visible light active semiconductor with a narrow band gap (2.3 eV) [15].

It appears evident why GdFeO_3 perovskite system has attracted a lot of interest for different applicative perspectives such as photo-catalysis, microwave communication, magnetic and magneto-optical storage, photovoltaic solar cell, and magnetic resonance imaging (MRI) or magneto fluid hyperthermia (MH) [16–18].

This wide variety of potential applications is motivated by different chemical and physical advantages offered by GdFeO_3 system. Indeed, Gd ferrites ceramics are non-toxic, highly stable, and chemically inert allowing for a largescale production favoured by their low price. Moreover, from the

microscopic point of view, the ABO_3 perovskite structure offers the possibility to selectively doping A and B sites, inducing structural distortions because of different ionic radii and oxidation states, thus, in turn modifying magnetic, optical, and transport properties. The high chemical and physical tunability is further enhanced by the use of facile synthesis routes producing nanometric sized ceramics. This small dimension allows inducing superparamagnetism, a crucial issue for biomedical applications [18].

Different synthesis methods can be fruitfully used to prepare nanosized Gd ferrites [3, 4, 7, 12, 14]. Nevertheless, at the nanoscale, it becomes fundamental, for widespread application, to maintain a fine control on different issues: (i) the desired distribution of cations, both native and dopants, on A and B sites, (ii) the desired oxidation states of ions, (iii) the proper oxygen stoichiometry, and (iv) the phase purity and homogeneity over the nanometric grains.

Thus, it is mandatory for nano-grained GdFeO_3 to deepen the knowledge about the cross-correlation between synthetic routes, different dopants on both sublattices, phase purity, and structural and magnetic properties [19, 20]. In particular, it could be interesting to probe the doping on both A and B sites with biocompatible, aliovalent non-magnetic ions, to influence the magnetic properties both directly and by the intermediation of structural effects the magnetic properties.

In the present paper, undoped and Ca- and Mg-(10 at.%) substituted GdFeO_3 were prepared by means of different synthesis routes, i.e. microwave assisted, sol-gel, and polyol synthesis, to possibly relate the magnetic and spectroscopic properties to peculiar structural features. The samples were thoroughly characterized by X-ray powder diffraction (XRPD), Scanning electron microscopy (SEM), and Micro-Raman spectroscopy. In this way, the formation of solid solutions was demonstrated and their particle shapes and sizes and vibrational properties were determined. SQUID magnetization measurements allowed to determine the magnetic character of the different samples and to put into evidence the eventual effect of substitution into the GdFeO_3 lattice.

2 Methods

2.1 Synthesis

Undoped and Ca- and Mg-substituted orthoferrite compounds were prepared with the following stoichiometries: GdFeO_3 , $\text{Gd}_{0.9}\text{Ca}_{0.1}\text{FeO}_3$, and $\text{GdFe}_{0.9}\text{Mg}_{0.1}\text{O}_3$. Each of them was synthesized by the three following methods:

1. Microwave: $\text{Gd}(\text{NO}_3)_3 \cdot 6\text{H}_2\text{O}$ and $\text{Fe}(\text{NO}_3)_3 \cdot 9(\text{H}_2\text{O})$ (and the eventual nitrate of the substituent cation Ca or Mg) were mixed in the proper amount with an excess of citric acid (2:1 mol amount with respect to the sum of cations moles) used as a propellant to start the combustion reaction assisted by the microwaves [21]. The mixed powders were ground, put into a ceramic crucible, and treated in a Milestone oven in air at 800 W for about 2 h (with a limit on the maximum temperature of 670 °C).
2. Sol–gel: $\text{Gd}(\text{NO}_3)_3 \cdot 6\text{H}_2\text{O}$, $\text{Fe}(\text{NO}_3)_3 \cdot 9(\text{H}_2\text{O})$ (and the eventual nitrate of the substituent cation) and citric acid in excess (2:1 mol amount with respect to the sum of those of cations) were dissolved in water. The solution was dried at about 80 °C on magnetic stirrer until a gel was obtained, then all the solvent was evaporated. The obtained powder was treated at 300 °C for 4 h to remove the organic components, then was ground, and heated at 700 °C for 10 h in oven.
3. Polyol reflux [22]: the proper amount of $\text{Gd}(\text{NO}_3)_3 \cdot 6\text{H}_2\text{O}$ and $\text{Fe}(\text{NO}_3)_3 \cdot 9(\text{H}_2\text{O})$ (and the eventual nitrate of the substituent cation) was added to 10 ml of ethylene glycol (EG). When the temperature had reached 110 °C, 5.6 mmol of KOH, dissolved in 10 ml of EG, was added. The temperature was further raised to 190 °C and maintained for 4 h. After cooling, the precipitate was isolated by centrifugation, washed three times with methanol, dried in oven at 100 °C overnight, and subsequently treated at 700 °C for 10 h.

In the following, the samples will be named GFO (GdFeO_3), GCFO ($\text{Gd}_{0.9}\text{Ca}_{0.1}\text{FeO}_3$), and GFMO ($\text{GdFe}_{0.9}\text{Mg}_{0.1}\text{O}_3$) followed by the acronym MW (microwave), SG (sol–gel), and P (polyol reflux) to specify the kind of synthesis.

2.2 Characterization techniques

X-ray powder diffraction (XRPD) measurements were performed by using a Bruker D5005 diffractometer with $\text{CuK}\alpha$ radiation (40 kV, 40 mA), graphite monochromator, and scintillation detector. The patterns were collected in air in the angular range 20–100°, with a step size of 0.03° and counting time of 16 s per step by using a silicon sample holder with low background. Rietveld structural and profile refinement was carried out by means of TOPAS 3.0 software [23] on the basis of the known crystal structure model of the orthorhombic GdFeO_3 perovskite. The instrumental broadening was determined by using as standard Si NBS. The peak profiles were modelled using a Lorentzian convolution approach allowing to determine the crystallite size values. During the refinement, the background coefficients, scale factor, zero error, lattice parameters, isotropic thermal factors and atomic positions were varied. The occupancies on both the cationic sites were allowed to vary, due to the sufficient difference in the X-ray atomic scattering factors, but of necessity constrained to one.

A Zeiss EVO MA10 scanning electron microscope (SEM) was used for the morphological study on gold-sputtered samples.

Micro-Raman measurements were carried out at room temperature using a Labram Dilor spectrometer equipped with an Olympus microscope HS BX40. The 632.8 nm light from a He–Ne laser was employed as the excitation radiation. The samples, mounted on a motorized *xy* stage, were tested with a $\times 50$ objective and with a laser spot of $\sim 2 \mu\text{m}$ diameter. The spectral resolution was about 1 cm^{-1} . Neutral filters with different optical densities were used to irradiate the samples at different light intensities, leading to power density values from 5×10^3 to $5 \times 10^5 \text{ W cm}^{-2}$. A cooled CCD camera was used as a detector and typical integration times were about 60 s. The sample phase homogeneity was verified by mapping the Raman spectra from different regions of each sample. The parameters of the Raman spectra were extracted by using best fitting procedures based on Lorentzian functions. In this way, the frequency, full width at half maximum, intensity and integrated intensity of the peaks were determined.

The magnetic characterization was carried out by means of a SQUID magnetometer. A 100 Oe magnetic

field (H) was applied to study the temperature dependence of the magnetization (M) in the range 2–300 K, in zero field cooling (ZFC) and field cooling (FC) regimes. Hysteresis loops were collected at 10 and 300 K with the magnetic field ranging between 0 and 10,000 Oe.

3 Results and discussion

3.1 XRPD and Rietveld refinement

The diffraction patterns of undoped GFO samples from the three syntheses evidence diffraction peaks at the same 2θ angles and with similar intensities, typical of highly crystalline orthorhombic GdFeO_3 (Card N. 47-0067), as shown in Fig. S1a. No impurity peaks are detected. Besides, the peak broadening of the three patterns is comparable, suggesting similar crystallite size values. So all the chosen synthesis methods are suitable to obtain high-purity samples at moderate temperatures, differently from other chemical routes requiring higher temperature [4, 7].

Similar observations can be performed for the Ca-doped GFO samples (Fig. S1b). The three patterns have the same diffraction peaks, with similar positions and broadening, also similar to those of GFO. No Ca-containing impurities were detected, suggesting, as expected, the high solubility of Ca into GdFeO_3 lattice and the formation of the solid solution.

Also for the patterns of GFMO samples, reported in Fig. S1c, a high similarity between them and those of pure and Ca-doped samples is evident, suggesting that all the syntheses can produce doped GdFeO_3 . The GFMO-P sample is practically pure, while in the MW and SG ones traces of Gd_2O_3 , as demonstrated by the small peak at about 29° , were detected [20].

In Fig 1a–c, as an example, the comparison between the experimental and calculated patterns on the basis of the perovskite orthorhombic $Pnma$ crystal structure is reported for undoped and doped samples obtained from polyol synthesis. The visual inspection suggests a good agreement, as demonstrated by the flat difference curve (grey) and also confirmed by the good agreement indices values (see Table 1) [24]. From Table 1, no clear trend for lattice parameters values can be detected by varying the sample stoichiometry, maybe due to the similarity of ionic radii values of the involved cations and to their small

amount [25]. For all the synthesized samples, nanocrystallites ranging between 22 and 45 nm are easily obtained [4]. The atomic coordinates, isotropic thermal factors and occupancies are reported in Table S1. For all the compositions, SG samples are smaller in grain size. Polyol synthesis provides slightly larger crystallite sizes for undoped and Ca-doped samples. For each synthesis, the larger crystallites are observed from Mg-doped samples.

3.2 SEM

SEM micrographs were collected on all the samples to verify the influence of synthesis and dopant on the morphology. From the inspection of SEM images in Fig. 2, a huge difference between the grain size and shape of samples from MW and SG and P syntheses was evident. This last one produces fine rounded particles that aggregate themselves in larger particles of tens of microns, difficult to fully visualize due to charging effects (notwithstanding the use of gold coating). The morphology is instead similar for MW and SG samples: particles reminiscent of combustion/decomposition processes originated by citric acid, with broken shapes and forming extended sheets are present [21]. The substituents do not produce any significant change in the morphology, which is clearly only controlled by the kind of synthesis. The crystallite sizes determined by XRPD refinements seem to have an opposite trend with respect to the grain sizes: they are larger for P synthesis with respect to MW and SG (Table 1). A comparison between crystallite and grain sizes is obviously difficult to be made, but on the basis of these evidences, we could hypothesize that the polyol synthesis allows improving the degree of crystal ordering, probably due to the milder reaction conditions and longer reaction times.

3.3 Raman spectroscopy

The Raman spectra at room temperature of undoped samples in the region $100\text{--}1800\text{ cm}^{-1}$ are reported in Fig. 3.

Gadolinium orthoferrites crystallize in the $Pnma$ orthorhombic space group (D_{2h} , 16) [26–28]. From the factor group analysis, among the 60 vibrational modes active at the Brillouin centre zone, the Raman activity consists of 24 modes with the following distribution: $7A_g + 5B_{1g} + 7B_{2g} + 5B_{3g}$. According to

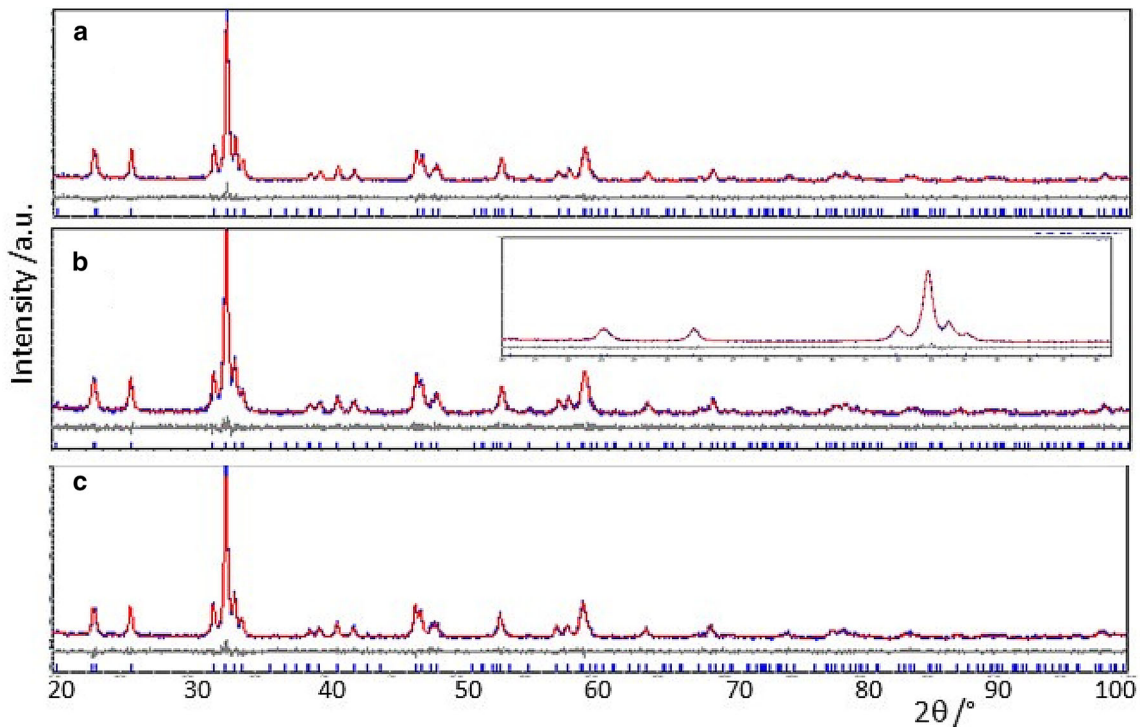


Fig. 1 Rietveld refinements on the diffraction patterns of **a** GFO-P, **b** GCFO-P, and **c** GMFO-P samples. The experimental pattern (blue) is compared with the calculated one (red); in the bottom, the difference curve (grey) and the bars of the expected peak positions

for GdFeO_3 are also shown. In the inset, as an example, an enlargement of the 20–35° angular region is shown for GCFO-P sample

Table 1 Main structural parameters and agreement indices obtained from Rietveld refinement of the synthesized GdFeO_3 sample patterns

		MW	SG	P
GFO				
Lattice parameters (Å)	a	5.3531(1)	5.3517(1)	5.3429(2)
	b	5.6137(1)	5.5893(2)	5.6031(1)
	c	7.6826(2)	7.6696(3)	7.6671(2)
Cry size (nm)		31.4(5)	22.6(4)	41.5(6)
$R_{\text{wp}}/\text{GoF}/R_{\text{B}}$		10.68/1.09/ 2.47	11.02/1.14/ 2.25	10.44/1.07/ 2.16
GCFO				
Lattice parameters (Å)	a	5.3549(1)	5.3332(1)	5.3442(1)
	b	5.5999(1)	5.5689(1)	5.5991(1)
	c	7.6738(3)	7.6611(2)	7.6729(2)
Cry size (nm)		31.2(4)	24.3(3)	33.2(3)
$R_{\text{wp}}/\text{GoF}/R_{\text{B}}$		10.94/1.11/ 1.43	10.93/1.09/ 1.69	10.58/1.06/ 1.68
GFMO				
Lattice parameters (Å)	a	5.3480(2)	5.3494(1)	5.3448(1)
	b	5.6129(1)	5.6055(2)	5.6025(2)
	c	7.6672(2)	7.6658(1)	7.6710(2)
Cry size (nm)		45.2(5)	38.7(4)	39.4(4)
$R_{\text{wp}}/\text{GoF}/R_{\text{B}}$		10.44/1.07/ 2.18	11.29/1.1/2.07	10.92/1.06/ 2.41

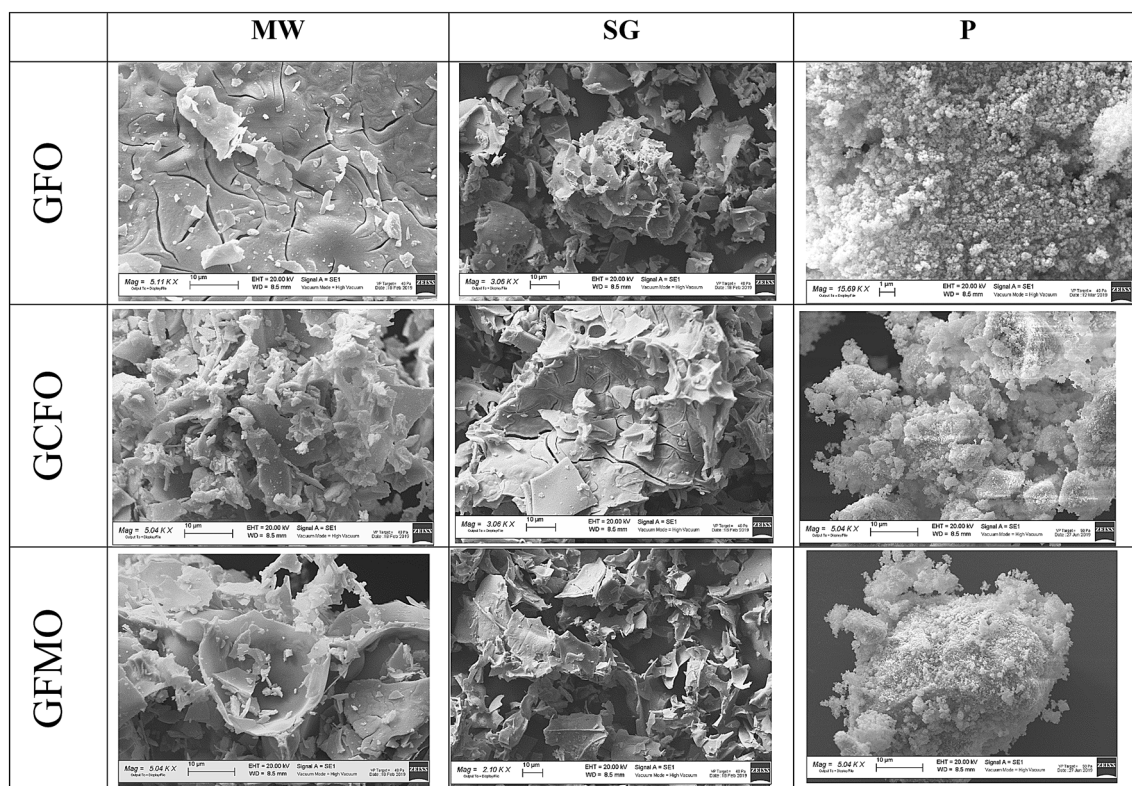


Fig. 2 SEM images collected on all the samples obtained by the three synthetic routes

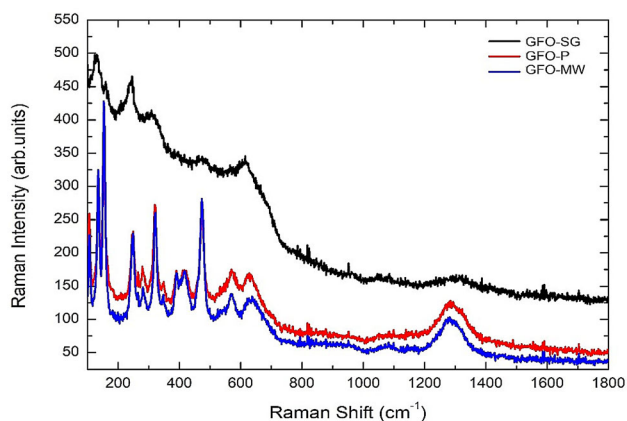


Fig. 3 Raman spectra of GFO samples at room temperature

the literature [27–30], the room temperature first-order Raman activity in polycrystalline GdFeO_3 is mainly expected in the region between 100 and 650 cm^{-1} . In particular, it is possible to discriminate (i) below 200 cm^{-1} the Raman features related to lattice modes involving Gd vibrations, (ii) between 200 and 400 cm^{-1} the contribution of different modes, reasonably ascribable to in-phase and out-of-phase FeO_6 rotations, (iii) between 400 cm^{-1} and 500 cm^{-1} the bending activity of $\text{O}(1)\text{--Fe--O}(2)$ and

stretching of $\text{Fe--O}(1)$ and/or $\text{Fe--O}(2)$ and (iv) above 600 cm^{-1} in-plane stretching modes. The different intensity of the modes relates to the symmetries and the most intense ones have usually A_g symmetry. The broadened band at about 1280 cm^{-1} can be endorsed as a two-phonon process related to the signal at about 630 cm^{-1} [28, 31].

This scenario appropriately describes that observed for GFO-MW and GFO-P samples. The spectra are characterized by sharp Raman features and many of the 24 predicted modes can be easily recognized, being the main Raman signals peaked at 105, 134, 153, 245, 321 and 474 cm^{-1} . These Raman signals display an almost symmetric shape and are accompanied by weaker and broadened features at around 281, 345, 390, 418, 567 and 630 cm^{-1} . No traces from impurity phases are detected over the whole $100\text{--}1800\text{ cm}^{-1}$ range, confirming that the organic compounds used during the synthesis have been completely dropped out. This is true also for GFO-SG sample, but, in this case, its Raman spectrum is characterized by a broad unresolved continuum extending up to 650 cm^{-1} . Raman structures, peaked at around 130, 242, 309, 472 and 615 cm^{-1} , emerge

over this continuum. Comparing the main Raman features of the undoped samples, it is clear that a high structural order can be deduced for GFO-MW and GFO-P samples, while this is not true for GFO-SG, whose Raman spectrum is rather similar to that of a glassy system. This behaviour seems to disagree with XRPD data, displaying instead a well-defined pattern, typical of GdFeO_3 in a similar fashion to the other two undoped samples. GFO-SG has slightly smaller average crystallite sizes, but it is hard to consider grain sizes of about 22 nm as responsible by themselves for this behaviour. Rather, we think that the peculiar results achieved for GFO-SG depend on the presence of a highly disordered shell around a more ordered core, while for GFO-MW and GFO-P, the crystalline order is maintained over the whole dimension of the grains. This situation is relevant for Raman scattering due to a higher sensitivity to the surface defectiveness with respect to X-ray radiation. At the considered wavelength and grain sizes, the penetration depth in Raman experiments allows to sample the whole grain depths and the structureless signal from the outer shell likely might mask and overwhelm the structured Raman signals from the inner core, further weakened by multiple photon scattering from the disordered surface layer.

In Fig. 4, the result of the best fitting procedure in the range $100\text{--}350\text{ cm}^{-1}$ on the Raman data for GFO-MW is reported. A very good interpolation has been obtained using six Lorentzian curves. In particular, FWHM values between 3 and 10 cm^{-1} are determined for all the Raman modes, suggesting a high crystallinity degree, comparable with the literature data [27].

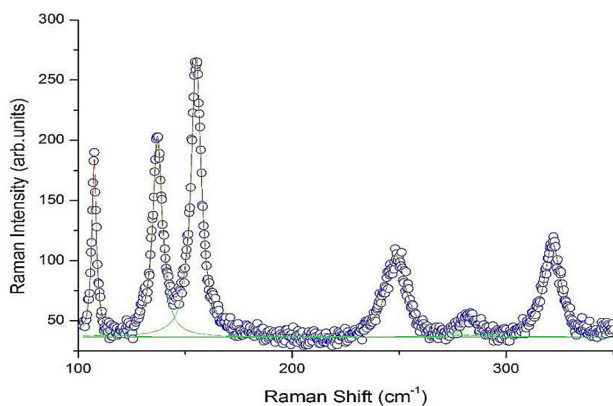


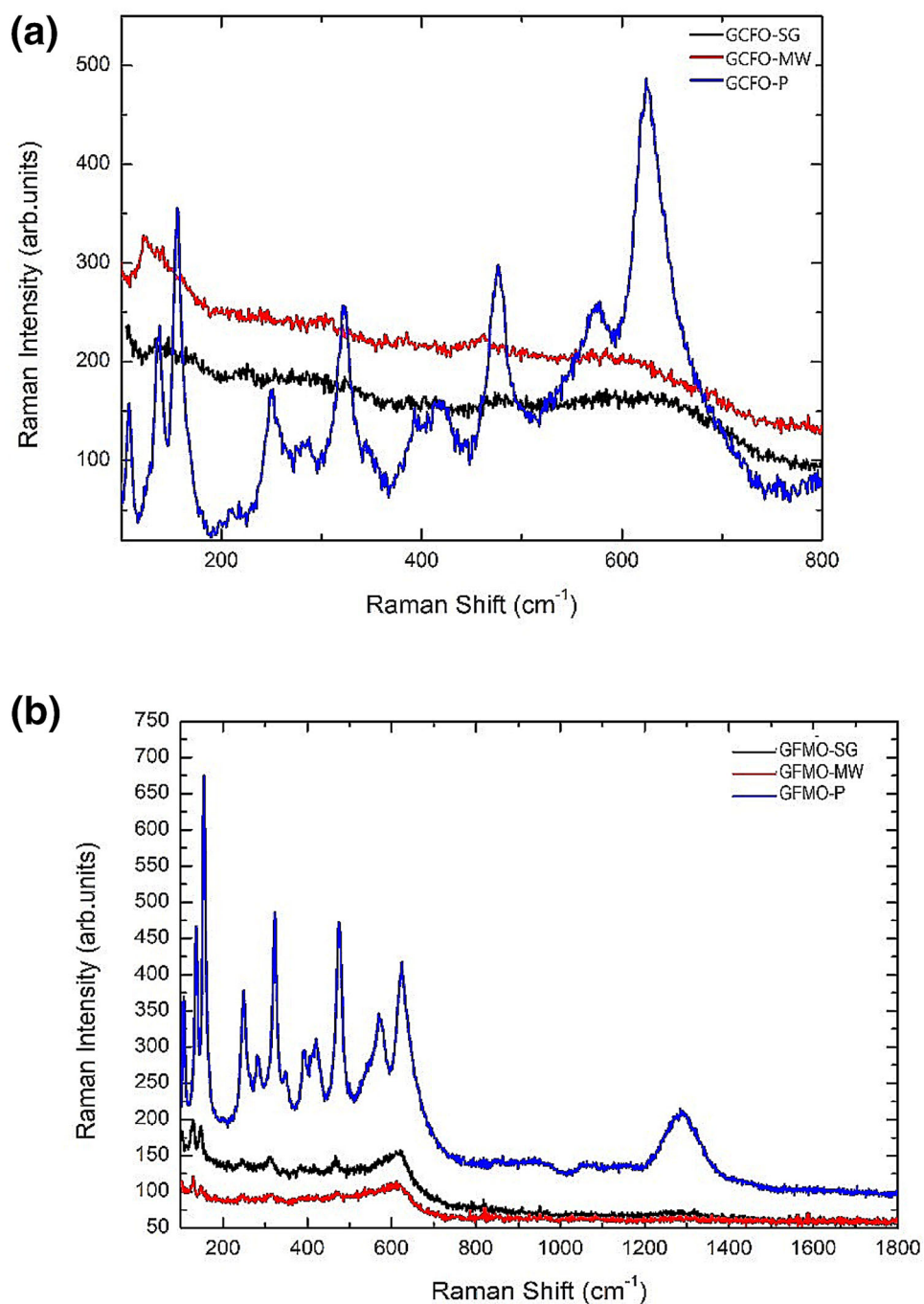
Fig. 4 Raman spectrum in the range $100\text{--}350\text{ cm}^{-1}$ for the GFO-MW sample and the result from the best fitting procedure (red line). Green lines represent each single lorentzian curve

The Raman spectra of doped samples (GCFO and GFMO) from the different synthetic routes are reported in Fig. 5a and b. The doping, regardless the cationic site substitution, causes very weak changes on the main features of Raman spectrum for samples from polyol synthesis. The whole Raman spectrum is quite similar to the undoped one, even if the FWHMs are about 20% larger. Both the expected Ca on Gd sites and Mg on Fe sites substitutions cause a relative intensity increase of the modes around 600 cm^{-1} , particularly for the mode at around 630 cm^{-1} . For GCFO, this effect is accompanied by a relative decrease in the Raman intensities of the normal modes involving Gd vibrations. These features seem to be consistent with an increase of disorder with doping, due to the presence of oxygen vacancies (formed to balance the lack of positive charges due to the substitution of Gd^{3+} and Fe^{3+} ions with Ca^{2+} and Mg^{2+} ones) accompanied by steric effects. The presence of vacancies introduces distortions in the octahedral units and this is the reason for the observed increase of the mode above 600 cm^{-1} .

The doped samples from MW and SG syntheses display a quite different behaviour from the P-doped samples: in fact, they are characterized by a very low Raman activity. In both cases (Ca or Mg doping), the Raman spectra consist of a weak and broadened continuum between 100 and 600 cm^{-1} with a glassy like behaviour, already observed for GFO-SG sample. The main Raman features of GdFeO_3 observed in undoped MW and P samples are strongly reduced and hardly recognizable. At lower energies, i.e. for the Gd-related modes, the doublet Raman structure is again present for GFMO, but not for GCFO, due to the direct modification on Gd sites.

The Raman yield appears almost quenched for Ca-doped samples. As already said, we think that a structureless and weaker Raman signal could be related to a very low crystallinity of the outer shell of the grains, but for Ca-doped samples, this could be also associated to the tendency of Ca ions to form more regular perovskites, such as CaTiO_3 , with cubic structure and 12-fold coordination. This can suggest that the substitution could locally change the coordination of cations, whose effects are reflected in the Raman spectrum. So, as well as XRPD, Raman spectroscopy also identifies the polyol synthesis as the most suitable to obtain well ordered and crystalline materials, both for undoped and substituted samples.

Fig. 5 Raman spectra of GCFO (a) and GFMO (b) samples obtained from the three synthetic routes



To better analyse the higher crystallinity degree of the samples obtained from P synthesis, Raman spectra were collected as a function of the position of the laser spot. The results on the GFMO-P sample are reported in Fig. 6, as an example.

The Raman signals are well stable and the crystalline phase does not change. From these data, we derived the average Raman spectra for GFO-P, GCFO-P and GFMO-P samples, that were processed

by best fitting procedures, in particular, at lower ($100\text{--}200\text{ cm}^{-1}$) and higher ($550\text{--}650\text{ cm}^{-1}$) energy regions deriving linewidths and peak positions. For GFO-P, the Raman modes at 134.5 and 153.1 cm^{-1} display linewidths of 7.1 and 8.3 cm^{-1} , respectively. From GCFO and GFMO samples, the linewidths of the same modes were calculated as 7.8 , 9.4 cm^{-1} and 7.1 , 8.4 cm^{-1} , respectively. These results are a net indication that Ca doping causes an effective

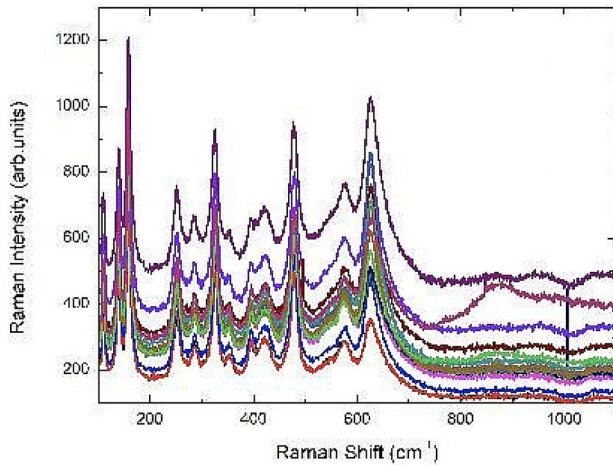


Fig. 6 Raman spectra collected on 15 points along a line of 30 μm on the GFMO-P sample

alteration on Gd sites, thus in turn validating the effectiveness of doping. From similar analyses on the higher energy mode (630 cm^{-1} in GFO-P), we obtained the same value for GCFO and a 3 cm^{-1} red shift for GFMO. The effect on the linewidths is more evident: 22.6 for GFO, 47.7 for GCFO and 70.9 cm^{-1} for GFMO. Also in this case, a correlation between dopant and sites involved in the substitution is detectable, but again we have to consider that Ca doping, as aliovalent substitution, can produce oxygen vacancies and thus might affect Fe–O stretching vibrations inside octahedral units because of distortions induced by vacancies. This reasoning motivated us to verify the stability of the Raman signals by varying the power of the laser, i.e. changing the laser-induced heating: the results on GCFO-P sample are reported in Fig. 7. The Raman bands do not change in position and shape by varying the laser power. From the comparison of the black traces, collected before and after the laser heating, a high intensity of the Raman mode at about 600 cm^{-1} , due to stretching vibration of FeO_6 octahedra, is evidenced. Similar results were obtained from GFMO-P, while for undoped sample this effect is markedly reduced. This indicates that octahedral units in doped samples are more sensitive to the laser heating, likely due to a thermal expansion more asymmetric than that in pure compound because of the disturbance of aliovalent dopants.

3.4 Magnetic results

GdFeO_3 shows a G-type canted antiferromagnetism resulting in a weak ferromagnetic behaviour [5–11]. These magnetic features come from the coexistence of two magnetic ions, Fe^{3+} and Gd^{3+} , giving rise to two antiferromagnetic (AF) sublattices with different paramagnetic to AF transition temperatures and with weak AF interlattices interactions [9, 10]. The spin-canted structure of Fe sublattice is related to the distorted orthorhombic perovskite structure [5, 6, 8].

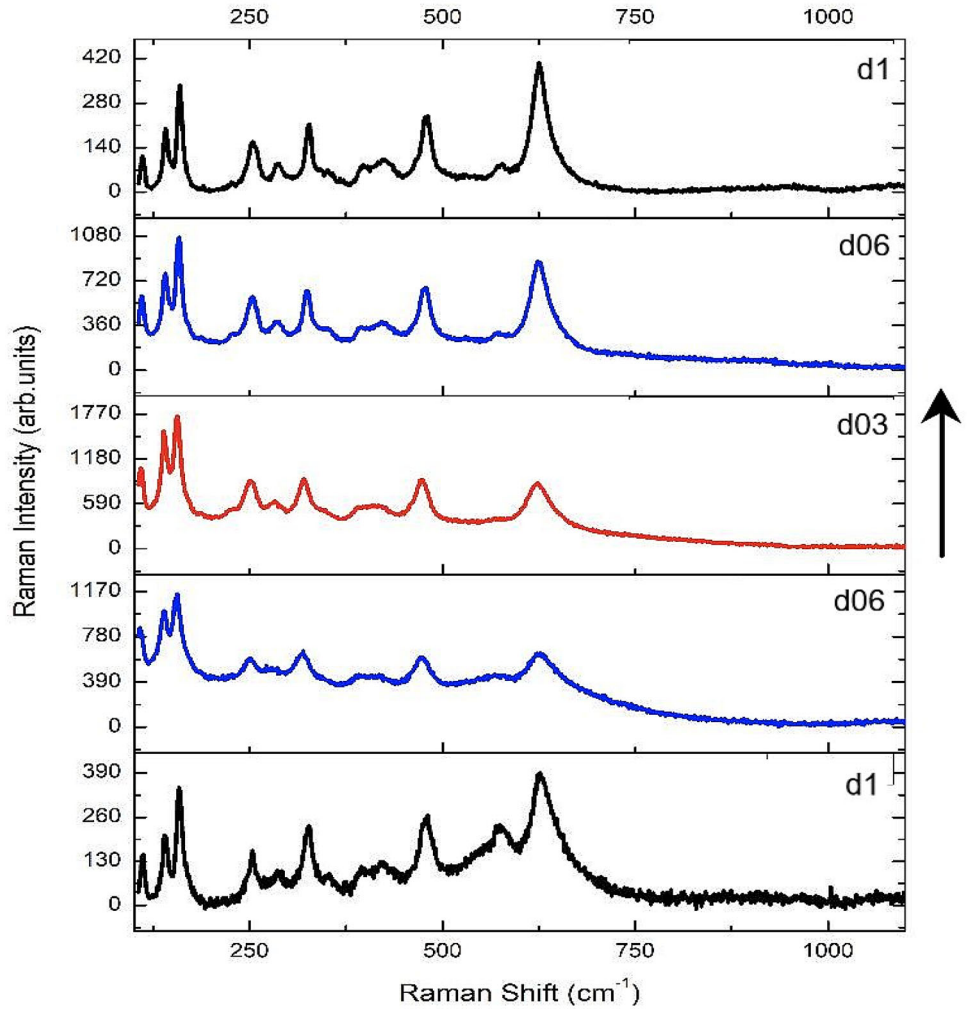
Samples investigated in this work do not show significant differences in the particles sizes and size distribution neither between undoped and doped orthoferrites nor between samples with the same chemical composition obtained from the three different synthesis routes (see Table 1). This allowed us to focus on how the peculiar magnetic properties observed for GdFeO_3 could be affected merely by a partial substitution of diamagnetic to magnetic (D/M) ions that necessarily modifies the paths of magnetic interactions, usually playing a crucial role on the magnetic behaviour of the compounds, especially in complex magnetic systems like GdFeO_3 . To this aim, we tried to perturb independently Gd and Fe sublattices by observing how the competition between the interactions could be driven in the different cases. We also tried to evaluate how the efficiency of the D/M ions substitution depends on the chosen synthesis procedure.

Concerning the P series, the study of the temperature dependence of magnetization in ZFC and FC regimes indeed evidenced major changes after both the D/M ions substitutions with respect to the GFO-P sample, while smaller differences were detectable between the two different kinds of substitution, as described below.

For GFO-P sample, a pure paramagnetic-like behaviour was observed, with ZFC and FC curves completely overlapped in the whole investigated temperature range. By using the Curie–Weiss law to extrapolate the Curie (C) and Weiss (θ) constant values from the experimental curve, we obtained $\mu_{\text{eff}} \cong 8.2\ \mu_{\text{B}}$ and a theta value of -6 K , confirming that the paramagnetic contribution comes from Gd^{3+} ions exhibiting very weak antiferromagnetic interactions.

We point out that a good quantitative agreement is found with what reported in [8], where the magnetic results obtained for accurately characterized good

Fig. 7 Raman spectra from different points of the GCFO-P sample. The signals were collected varying the intensity, introducing neutral filters with variable optical density (DO). The laser beam power varied from $5 \times 10^4 \text{ W/cm}^2$ (d_1) to $5 \times 10^5 \text{ W/cm}^2$ (d_0)



quality GdFeO_3 nanopowders ($> 40 \text{ nm}$) are described.

The ZFC and FC M vs T curves obtained for GFO-P sample, together with those of GCFO-P and GFMO-P, are shown in Fig. 8. After doping, more complex M vs T curves are disclosed, with a marked departure from the pure paramagnetic-like trend. Indeed, for Ca doping, the magnetic properties strongly depend on the different thermal history: ZFC and FC curves separate below RT, at a temperature that here we call T_{irr} (irreversibility temperature), as usually it occurs when magnetic domains are present, while the paramagnetic-like behaviour still dominates at low temperatures. Indeed, magnetic domains formation could be favoured by the interruption of the AF interactions paths between magnetic ions (Gd-Gd and Gd-Fe) because of the expected substitution of diamagnetic Ca^{2+} to magnetic Gd^{3+} ions. We should also consider that the different oxidation states and

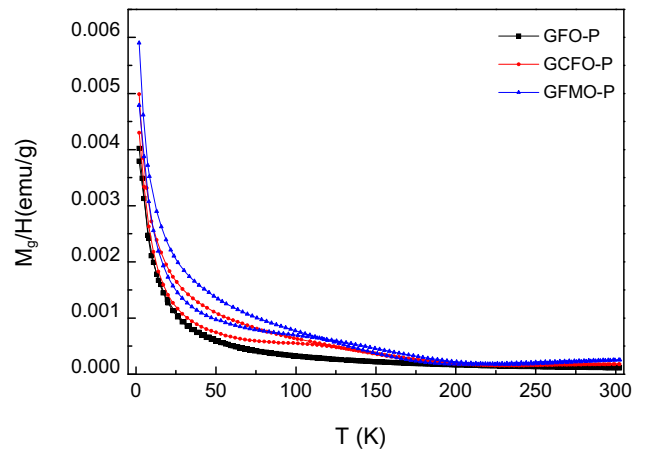


Fig. 8 ZFC and FC M vs T curves for samples obtained from P synthesis

the slightly larger ionic radius of Ca^{2+} with respect to Gd^{3+} ions (1.12 \AA against 1.05 \AA) [25], respectively, induce variations in charge balance and perturb the

local symmetry leading to a general increase of structural disorder, as already evidenced by Raman results (see par. 3.3).

A further complex behaviour is observed in the case of Mg substitution (Fig. 8). This is not surprising because the Mg^{2+} insertion is expected to occur on Fe^{3+} sites, thus affecting the main magnetic sublattice: the magnetic behaviour of the compound is in fact led from the super-exchange interactions between Fe^{3+} ions. We point out that also in this case a different oxidation state and a slightly larger ionic radius pertain to Mg^{2+} with respect to Fe^{3+} (0.72 Å against 0.645 Å).

The effects of Mg substitution on Fe sites are strongly supported by Raman observations: Mg insertion indeed affects the Fe–O peaks broadening suggesting octahedra distortions. In turn, also, Fe–Fe paths are clearly influenced and the material departs from the AF behaviour by the introduction of multiple domains that could be reasonably at the base of the complex intersections between ZFC and FC curves.

Let us now consider the effect of the same D/M ions substitutions for the compounds prepared via microwave-assisted combustion synthesis.

The related M vs. T curves, reported in Fig. 9, clearly show that, already for GFO-MW, ZFC and FC curves separate below RT. An analogous behaviour of M vs. T curves, with the same range of magnetization absolute values, was observed for a pure GdFeO_3 sample prepared via solid-state synthesis [32].

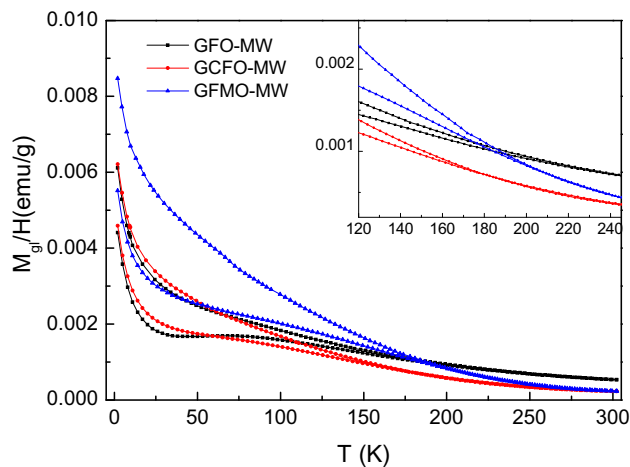


Fig. 9 ZFC and FC M vs T curves for samples obtained from MW synthesis. The inset shows an enlargement to better evaluate the differences in χ_0 and T_{irr} for the samples

At first glance, the different behaviour of M vs. T curves recorded for GFO-P and GFO-MW samples could be ascribed to the kind of synthesis. The rapid formation of the product induced by the MW-assisted combustion could indeed favour a generally higher disorder degree that in turn could directly give rise to magnetic domains according to a displacement from the proper arrangement of the paths of interactions, similar to what observed for the doped P samples. However, Raman results show no significant differences in the order degree between the two undoped GFO samples. In addition, for GFO-MW, we can also observe a markedly higher χ_0 value with respect to GFO-P (Fig. 8). This suggests that traces of an ordered magnetic phase could be present and could give rise to the observed thermal history dependence of magnetization below room temperature. Indeed, the presence of traces of spurious Fe-containing magnetic phases cannot be definitely excluded in this kind of compounds, even if the absence of the typical spurious magnetic phases in Raman spectra could suggest the intrinsic character of this behaviour.

For the MW series, after the D/M ions substitutions, slightly different T_{irr} values and markedly lower χ_0 values were detected from M vs. T curves with respect to GFO-MW (Fig. 9). On the other hand, our Raman measurements showed a lowering of Raman activity as consequence of doping, suggesting the introduction of structural disorder that could favour the observed magnetic behaviour, analogously to what occurs for the P series.

We tried to deepen the understanding of the observed magnetic features of the MW series by collecting hysteresis cycles at temperatures higher and lower than T_{irr} , in particular, at room temperature and 10 K. The cycles for the three samples, compared in Fig. 10a (at room temperature) and 10b (at 10 K), appear as the sum of two contributions, possibly ascribable to the two different magnetic sublattices.

At room temperature (Fig. 10a), a linear behaviour, referable to the paramagnetic trend, is overlapped to a S-shaped cycle, more evident for the GFO-MW sample. The higher M value of the S-shaped part observed for GFO-MW reflects the higher χ_0 value of the M vs. T curve. Negligible coercive fields are revealed: less than 10 Oe for GFO-MW and between 10 and 20 Oe for GCFO-MW and GFMO-MW samples.

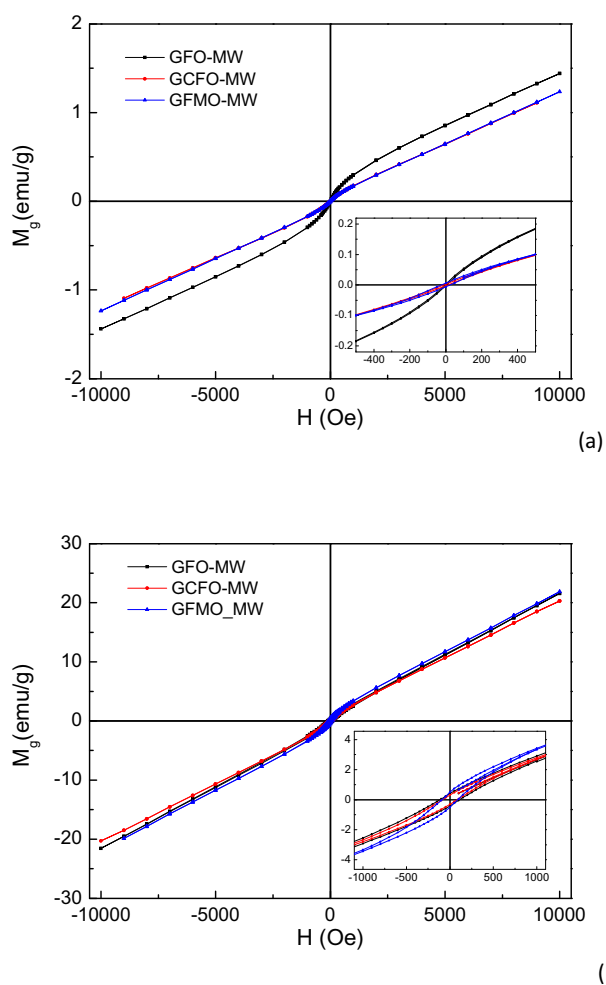


Fig. 10 Hysteresis cycles recorded for the MW samples at room temperature (a) and 10 K (b)

At 10 K (Fig. 10b), the linear paramagnetic trend is superimposed to an open cycle. In this case, a 115 Oe coercive field is recorded for GFO-MW, while for doped samples, a coercive field of 85 Oe is observed. The different values of coercive field between GFO-MW and the doped MW samples seem to support the different origin of magnetic domains in undoped and doped samples.

The non-linear part of the cycles could be in principle referred to superparamagnetic behaviour, but no conclusive evidence of intrinsic character is found. According to the literature, it could be due to the presence of traces of ferromagnetic-like impurities that, for nano-grained samples, can just give rise to superparamagnetic contribution. However, as already observed, Raman measurements do not

evidence magnetic impurities, such as iron or gadolinium oxides, as well as XRPD.

The separation of the two contributions to the hysteresis cycles can give some more information on the kind of D/M ions substitution. By fitting the linear part, the same value of paramagnetic susceptibility is obtained for pure and Mg-doped samples, both at room temperature and at 10 K, while a lower value is always obtained for Ca substitution. This means that the paramagnetic susceptibility is not affected when Mg substitution occurs, contrary to what happens for Ca substitution, confirming that Ca ions mainly disturb the Gd sublattice, paramagnetic in the whole investigated temperature range.

A different behaviour concerns the saturation magnetization of the hysteretic contribution. At room temperature, after the subtraction of the linear part, very similar cycles are obtained for the doped samples ($M_s \cong 0.06$ emu/g), while a higher M_s value (about 0.27 emu/g) is obtained for the GFO-MW. At 10 K GFO-MW and GCFO-MW samples reveal a similar value while an important increase of saturation value characterizes GFMO-MW sample. It is worth to notice that the traces of Gd_2O_3 revealed in GFMO-MW sample should not affect the saturation magnetization values because no ferromagnetic-like contribution is expected from Gd_2O_3 nanoparticles [33]. Thus, it can be concluded that also for the MW series Mg substitution affects, in a complex way, the main Fe magnetic sublattice, like in the case of P series.

Magnetization measurements performed on samples prepared via SG synthesis reveal an even more complex magnetic behaviour. This is evident in Fig. 11, showing a comparison between ZFC and FC M vs. T curves for the three Ca-doped samples obtained from the different syntheses considered in this work. Among them, GCFO-SG sample is the only one with not negligible coercive field already at room temperature, as shown in the inset of Fig. 11.

These observations agree with the Raman findings and support that the structural disorder play an essential role in determining the magnetic response in these compounds.

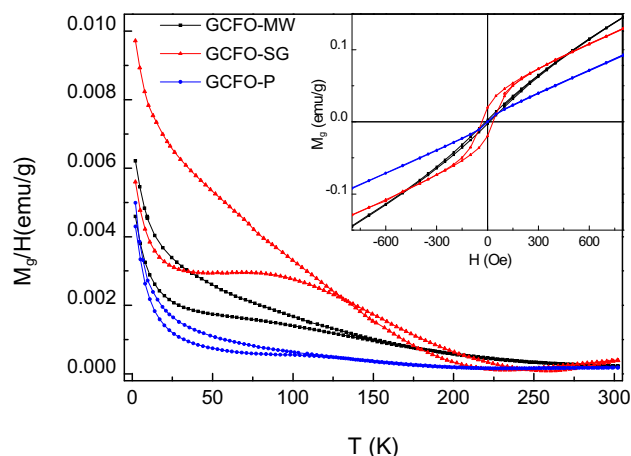


Fig. 11 ZFC and FC M vs T curves for Ca/Gd-substituted samples obtained from the three synthesis procedures. In the inset: room temperature hysteresis cycle for all the Ca-doped samples

4 Conclusions

In the present paper, all the samples of GdFeO_3 , undoped and doped with Ca and Mg ions, obtained from the three synthetic routes have nanometric sizes between 20 and 45 nm and similar lattice parameters. The morphology of the compounds is clearly related to the kind of synthesis and, among them, the polyol one appears to be the most suitable to obtain well ordered and crystalline materials, both for undoped and substituted samples.

XRPD, Raman spectroscopy, and magnetization results allowed us to demonstrate that Ca and Mg ions easily substitute on Gd and Fe sites, respectively, of GdFeO_3 perovskite lattice. The resulting magnetic properties were very complex. The diamagnetic Ca and Mg dopants seem to interrupt the paths of AF interactions between magnetic ions and their lower oxidation state and higher ionic radius with respect to Gd- and Fe-induced charge balance variations with consequent formation of oxygen vacancies and structural disorder that seem to be mainly responsible for the magnetic activity disturbance. The magnetic features evidence a superparamagnetic behaviour, but an intrinsic superparamagnetism of GdFeO_3 as a consequence of its nanometric sizes is not definitely demonstrated. Indeed, great attention should be paid to traces of magnetic impurities, particularly when iron is involved as in this case.

Acknowledgements

We thank Dr. Alessandro Girella for SEM measurements. Marco Moscardini is gratefully acknowledged for his precious technical support concerning the correct operation of the SQUID device.

Funding

Open access funding provided by Università degli Studi di Pavia within the CRUI-CARE Agreement. The paper does not receive any funding.

Availability of data and material

The datasets generated during the current study are available from the corresponding author on reasonable request.

Compliance with ethical standards

Conflict of interest The authors declare that they have no conflict of interest.

Electronic supplementary material: The online version of this article (<https://doi.org/10.1007/s10854-020-04374-8>) contains supplementary material, which is available to authorized users.

Open Access This article is licensed under a Creative Commons Attribution 4.0 International License, which permits use, sharing, adaptation, distribution and reproduction in any medium or format, as long as you give appropriate credit to the original author(s) and the source, provide a link to the Creative Commons licence, and indicate if changes were made. The images or other third party material in this article are included in the article's Creative Commons licence, unless indicated otherwise in a credit line to the material. If material is not included in the article's Creative Commons licence and your intended use is not permitted by statutory regulation or exceeds the permitted use, you will need to obtain permission directly from the copyright holder. To view a copy of this licence, visit <http://creativecommons.org/licenses/by/4.0/>.

References

- V.M. Goldschmidt, Die Gesetze der Kristallochemie. *Naturwissenschaften* **14**, 477–485 (1926)
- S. Geller, Crystal structure of gadolinium orthoferrite GdFeO₃. *J. Chem. Phys.* **24**, 1236–1239 (1956)
- S. Sahoo, P.K. Mahapatra, R.N.P. Choudhary, M.L. Nandagowami, A. Kumar, Structural, electrical and magnetic characteristics of improper multiferroic: GdFeO₃. *Mat. Res. Express* **3**, 065017 (2016)
- B.J. Prakash, B.H. Rudramadevi, S. Buddhudu, Analysis of ferroelectric, dielectric and magnetic properties of GdFeO₃ nanoparticles. *Ferroelectr. Lett. Sect.* **41**, 110–122 (2014)
- Y. Tokunaga, N. Furukawa, H. Sakai, Y. Taguchi, T. Arima, Y. Tokura, Composite domain walls in a multiferroic perovskite ferrite. *Nat. Mater.* **8**, 558 (2009)
- C.S. Vandana, B.H. Rudramadevi, Effect of Cu²⁺ substitution on the structural, magnetic and electrical properties of gadolinium orthoferrite. *Mat. Res. Express* **5**, 046101 (2018)
- L. Jiang, S. Yang, M. Zheng, H. Chen, A. Wu, Synthesis and magnetic properties of nanocrystalline Gd₃Fe₅O₁₂ and GdFeO₃ powders prepared by sol–gel auto-combustion method. *Mat. Res. Bull.* **104**, 92–96 (2018)
- S. Mathur, H. Shen, N. Lecerc, A. Kjekshus, H. Fjellvåg, G.F. Goya, Nanocrystalline orthoferrite GdFeO₃ from a novel heterobimetallic precursor. *Adv. Mater.* **14**, 1405–1409 (2002)
- M. Das, S. Roy, P. Mandal, Giant reversible magnetocaloric effect in a multiferroic GdFeO₃ single crystal. *Phys. Rev. B* **96**, 174405 (2017)
- J.D. Cashion, A.H. Cooke, D.M. Martin, M.R. Wells, Magnetic interactions in gadolinium orthoferrite. *J. Phys. C* **3**, 1612–1620 (1970)
- H. Xu, X. Hu, L. Zhang, Generalized low-temperature synthesis of nanocrystalline rare earth orthoferrites LnFeO₃ (Ln = La, Pr, Nd, Sm, Eu, Gd). *Cryst. Growth Des.* **8**, 2061–2065 (2008)
- Y. Zhang, A. Zheng, X. Yang, H. He, Y. Fan, C. Yao, Cubic GdFeO₃ particle by a simple hydrothermal synthesis route and its photoluminescence and magnetic properties. *Cryst. Eng. Commun.* **14**(8432), 8439 (2012)
- A. Scrimshire, A. Lobera, A.M.T. Bell, A.H. Jones, I. Sterianou, S.D. Forder, P.A. Bingham, Determination of Debye temperatures and Lamb–Mössbauer factors for LnFeO₃ orthoferrite perovskites (Ln = La, Nd, Sm, Eu, Gd). *J. Phys.* **30**, 105704 (2018)
- S. Middey, P. Mahadevan, D.D. Sarma, Dependence of magnetism on GdFeO₃ distortion in the *t*2g system ARuO₃ (A = Sr, Ca). *Phys. Rev. B* **83**, 014416 (2011)
- X.H. Zhu, X.B. Xiao, X.R. Chen, B.G. Liu, Electronic structure, magnetism and optical properties of orthorhombic GdFeO₃ from first principles. *RSC Adv.* **7**, 4054–4061 (2017)
- N.F. Atta, A. Galal, E.H. El-Ads, *Perovskite Materials - Synthesis, Characterisation, Properties, and Applications* (Intech Open Publication, London, 2016)
- J.J. Choi, S.J.L. Billinge, Perovskites at the nanoscale: from fundamentals to applications. *Nanoscale* **8**, 6206–6208 (2016)
- M. Saeed, W. Ren, A. Wu, Therapeutic applications of iron oxide based nanoparticles in cancer: basic concepts and recent advances. *Biomater. Sci.* **6**, 708–725 (2018)
- A. Panchwancee, V. Raghavendra Reddy, A. Gupta, A. Bharathi, D.M. Phase, Study of local distortion and spin reorientation in polycrystalline Mn doped GdFeO₃. *J. Alloys Comp.* **745**, 810–816 (2018)
- C.S. Vandana, J. Guravamma, B. Hemalatha Rudramadevi, Synthesis and dielectric properties of Zn doped GdFeO₃ ceramics. *IOP Conf. Ser.* **149**, 012180 (2016)
- M. Bini, C. Tondo, D. Capsoni, M.C. Mozzati, B. Albin, P. Galinetto, Superparamagnetic ZnFe₂O₄ nanoparticles: the effect of Ca and Gd doping. *Mat. Chem. Phys.* **204**, 72–82 (2018)
- F. Söderlind, M.A. Fortin, R.M. Petoral Jr., A. Klasson, T. Veres, M. Engström, K. Uvdal, P. Käll, Colloidal synthesis and characterization of ultrasmall perovskite GdFeO₃ nanocrystals. *Nanotechnology* **19**, 085608 (2008)
- A.X.S. Brucker, Topas V 3.0. General profile and structural analysis software for powder diffraction data. *J. Appl. Cryst.* **51**, 210–218 (2005)
- B.H. Toby, R factors in Rietveld analysis: how good is good enough? *Powder Diffr.* **21**, 67–70 (2006)
- R.D. Shannon, Revised effective ionic radii and systematic studies of interatomic distances in halides and chalcogenides. *Acta Cryst.* **A32**, 751–767 (1976)
- I.S. Smirnova, Normal modes of the LaMnO₃ Pnma phase: comparison with LaCuO₃ Cmca phase. *Phys. B* **262**, 247–261 (1999)
- M.C. Weber, M. Guennou, H.J. Zhao, J. Íñiguez, R. Vilarinho, A. Almeida, J.A. Moreira, J. Kreisel, Raman spectroscopy of rare-earth orthoferrites RFeO₃ (R = La, Sm, Eu, Gd, Tb, Dy). *Phys. Rev. B* **94**, 2144103 (2016)
- A. Panchwancee, S.K. Upadhyay, N.P. Lalla, V.G. Sathe, A. Gupta, V. Raghavendra Reddy, Low-temperature Raman, high magnetic field ⁵⁷Fe Mossbauer, and X-ray diffraction study of magnetodielectric coupling in polycrystalline GdFeO₃. *Phys. Rev. B* **99**, 064433 (2019)
- M. Romero, R.W. Gómez, V. Marquina, J.L. Pérez-Mazariago, R. Escamilla, Synthesis by molten salt method of the AFeO₃ system (A = La, Gd) and its structural, vibrational and

- internal hyperfine magnetic field characterization. *Phys. B* **443**, 90–94 (2014)
30. V. Srinu Bhadram, B. Rajeswaran, A. Sundaresan, C. Narayana, Spin-phonon coupling in multiferroic RCrO (Lu, Gd, Eu, Sm): a Raman study. *Europhys. Lett.* **101**, 17008 (2013)
 31. R.J. Wiglusz, K. Kordek, M. Małecka, A. Ciupa, M. Ptak, R. Pazik, P. Pohl, D. Kaczorowski, A new approach in the synthesis of $\text{La}_{1-x}\text{Gd}_x\text{FeO}_3$ perovskite nanoparticles – Structural and magnetic characterization. *Dalton Trans.* **44**, 20067–20074 (2015)
 32. Y.J. Ke, X.Q. Zhang, J.F. Wang, Z.H. Cheng, Giant magnetic entropy change in gadolinium orthoferrite near liquid hydrogen temperature. *J. Alloys Compd.* **739**, 897–900 (2018)
 33. E.L. Correa, B. Bosch-Santos, F.H.M. Cavalcante, B.S. Correa, R.S. Freitas, A.W. Carbonari, M.P.A. Potiens, Properties of Gd_2O_3 nanoparticles studied by hyperfine interactions and magnetization measurements. *AIP Adv.* **6**, 056112 (2016)

Publisher's Note Springer Nature remains neutral with regard to jurisdictional claims in published maps and institutional affiliations.